Journal of Science and Technology in Civil Engineering, NUCE 2021. 15 (3): 1–12

ANALYSIS OF NON-UNIFORM HEXAGONAL CROSS-SECTIONS FOR THIN-WALLED FUNCTIONALLY GRADED BEAMS USING ARTIFICIAL NEURAL NETWORKS

Dieu T. T. Do[a], Tan-Tien Nguyen[b], Quoc-Hung Nguyen[b], Tinh Quoc Bui[c,*]

[a] *Duy Tan Research Institute for Computational Engineering, Duy Tan University, 254 Nguyen Van Linh street, Da Nang city, Vietnam*
[b] *Faculty of Engineering, Vietnamese-German University, Le Lai Street, Thu Dau Mot City, Binh Duong province, Vietnam*
[c] *Department of Civil and Environmental Engineering, Tokyo Institute of Technology, Tokyo, Japan*

Article history:
Received 12/07/2021, Revised 23/07/2021, Accepted 26/07/2021

Abstract

We study static mechanical behavior of non-uniform hexagonal cross-sections for thin-walled functionally graded beams using a non-traditional computational approach based on artificial neural network. One of the main objectives of our approach is to save the computational cost for the optimization process, which is usually time-consuming by using traditional methods such as finite element method (FEM). In this study, 1000 data sets randomly generated by the FEM through iterations are used for the training process to get optimal weights. Based on these obtained optimal weights, beam behaviors under the changes in material distribution through thickness could then be predicted. In this model, the ANN's inputs are the gradation index of the power-law distribution and thickness, while the outputs are compliance and beam displacements. The computed results are verified against those derived from the FEM.

Keywords: artificial neural network; hexagonal cross-section; functionally graded materials; thin-walled beam.

https://doi.org/10.31814/stce.nuce2021-15(3)-01

---

1. Introduction

Thin-walled structures have been widely applied in a variety of engineering applications including building construction, storage racks, automotive, and aircraft [1, 2]. The functionally graded materials (FGMs) with superior metal and ceramic continuity which aid in the elimination of abrupt transitions between distinct materials have been introduced. Thermal and flexural resistances are among their advantages, and thin-walled structures integrated with FGMs have been developed in many studies [3–6].

Many studies have previously been developed such as a well-known study of Vlasov [7] or Tews et al. [8] who proposed an automatic hp-adaptive finite element method (FEM) for efficiently describing geometries and that allowed simulation on a variety of structures. In the analysis of thin-walled structures, Rank et al. [9] used a finite cell method with a fictitious domain approach which uses

*Corresponding author. *E-mail address:* tinh.buiquoc@gmail.com (Bui, T. Q.)

higher-order shape functions. Though solutions found in the literature have demonstrated to be quite effective, there are still some issues where natural behavior aspects have not been fully considered, for example higher-orders of distortion as it occasionally takes more effort to complete. Besides, polygonal cross-sections have become increasingly appealing to many recent studies and a more thorough analysis of their mechanical behaviors is necessary. As a result, Nguyen et al. [10, 11] developed design technique for thin-walled FG beams with polygonal cross-sections that takes into account higher-order warping, distortion and anisotropy of FGMs. In their works, the FEM was used to model the structures. However, such method is computationally expensive for numerical analysis.

Besides, ANN is a computational model based on the architecture of biological neural networks that aims to simulate how humans learn from data. In most cases, an ANN is made up of layers: hidden, input, and output, each of which is made up of nodes. ANN has been widely used in a variety of fields, including robots, computer vision, translation, speech recognition, self-driving cars, and engineering mechanics. In particular, Vesperini et al. [12] proposed an ANN for multi-room speaker localization, in which convolutional neural networks and multi-layer perceptron architectures were investigated. In the engineering field, Do et al. [13] presented an ANN for material optimization of functionally graded plates under buckling load or free vibration. Le et al. [14] proposed a risk assessment framework using ANN technique. The framework with successful model has been used as a tool to help construction companies assess risk and evaluate its impact on project profitability. Besides, a hybrid deep learning algorithm was proposed for structural damage detection tasks [15]. That approach aimed to reduce required resources and has the capability to deal with different damage levels. Moreover, Truong et al. [16] suggested Deep Neural Network for estimation of ultimate load factor of nonlinear inelastic steel truss. Based on obtained numerical results, the high accuracy of the method was verified. And several other studies in the engineering field were shown in the literature as [17, 18]. ANN's effectiveness and accuracy have been confirmed through above studies.

Therefore, in this study, ANN is proposed to predict the behavior of non-uniform hexagonal cross-sections for thin-walled FG beams in the first time. Because, for optimization problems, to identify a globally optimal solution, a significant number of structural analyses is required; consequently, numerical analysis of the thin-walled FG beams based on FEM must be performed numerous times. As a result, there is a significant increase in the cost of computing. To overcome this limitation, artificial neural network (ANN) is proposed as an efficient way to predict the behavior of thin-walled FG beams quickly. The ANN is used in place of FEM to reduce computational time while maintaining the quality of the results. In which, 1000 data sets for training process are generated randomly by FEM through iterations. The number of data sets is significant smaller than the number of structural analyses which are required in the optimization problems. After the training process, beam behaviors under changes in material distribution through thickness and thickness can be predicted quickly without using FEM. In addition, the influence of the number of hidden layers and epochs in an ANN on accuracy and computational cost is considered. The effectiveness and reliability of the proposed approach are demonstrated through numerical examples in terms of accuracy and computational cost.

2. Theory of thin-walled beam

2.1. Kinematics

A combination of higher-order modes and 1D deformations are used to define 3D displacements of an arbitrary point on a cross-section in the axial direction. Governing equations are established using the principle of the minimum potential energy, based on stress-strain relations, stress resultants

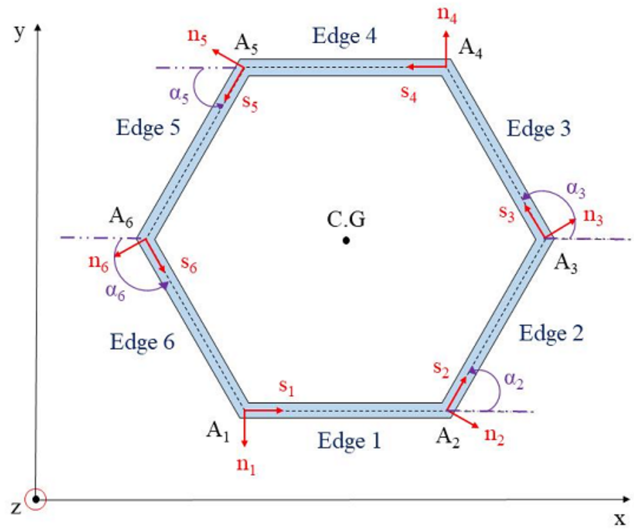

Figure 1. Geometries and coordinates of a thin-walled hexagonal cross-section

and constitutive equations. The contour displacements or 3D middle plane on the general hexagonal cross-section, as depicted in Fig. 1, can be determined as follows:

$$\bar{\mathbf{u}} = \mathbf{\Psi} \cdot \mathbf{U} \tag{1}$$

in which

$$\bar{\mathbf{u}} = \begin{Bmatrix} \bar{u}_n \\ \bar{u}_s \\ \bar{u}_z \end{Bmatrix} \tag{2}$$

where s, n-axes are, which are in-plane coordinates, tangential and normal to the mid- surface of a cross-section, respectively; and z-axis parallels to the beam's axial direction. In Fig. 1, α_i symbolizes the angle between the edge i^{th} and x-axis.

The shape functions described by s variation in the contour direction of a cross-section, which include conventional rigid bodies and higher-order deformations, are given as:

$$\mathbf{\Psi} = \begin{Bmatrix} \mathbf{\Psi}_n(s) \\ \mathbf{\Psi}_s(s) \\ \mathbf{\Psi}_z(s) \end{Bmatrix} \tag{3}$$

The displacements for any arbitrary position on a cross-section can be simply calculated using Kirchhoff-Love assumptions as follows:

$$\mathbf{u}^* = \begin{Bmatrix} u_n^* \\ u_s^* \\ u_z^* \end{Bmatrix} = \begin{Bmatrix} \bar{u}_n \\ \bar{u}_s - n\dfrac{\partial \bar{u}_n}{\partial s} \\ \bar{u}_z - n\dfrac{\partial \bar{u}_n}{\partial z} \end{Bmatrix} \tag{4}$$

In comparison to other thin-walled theories, shear strains in the mid-plane are probably negligible as an acceptable solution due to its complexity in multi-dimensional and multi-variable issues. These effects are, however, taken into consideration in our research in order to achieve more accurate results and properly represent the behavior of the thin-walled FG beam. In the case of planar stress, the strain vector can be approximated as:

$$\epsilon = \begin{Bmatrix} \epsilon_s \\ \epsilon_z \\ \gamma_{sz} \end{Bmatrix} = \begin{Bmatrix} \dfrac{\partial u_s^*}{\partial s} \\ \dfrac{\partial u_z^*}{\partial z} \\ \dfrac{\partial u_z^*}{\partial s} + \dfrac{\partial u_s^*}{\partial z} \end{Bmatrix} \simeq \begin{Bmatrix} \left(\dfrac{\partial \mathbf{\Psi}_s(s)}{\partial s} - n\dfrac{\partial^2 \mathbf{\Psi}_n(s)}{\partial s^2}\right)\cdot \mathbf{U} \\ \mathbf{\Psi}_z(s)\dfrac{\partial \mathbf{U}}{\partial z} - n\mathbf{\Psi}_n(s)\dfrac{\partial^2 \mathbf{U}}{\partial z^2} \\ \mathbf{\Psi}_s(s)\dfrac{\partial \mathbf{U}}{\partial z} + \dfrac{\partial \mathbf{\Psi}_z(s)}{\partial s}\cdot \mathbf{U} - 2n\dfrac{\partial \mathbf{\Psi}_n(s)}{\partial s}\dfrac{\partial \mathbf{U}}{\partial z} \end{Bmatrix} \tag{5}$$

In this study, a sandwich material is used in which the ceramic material at the middle plane is specified by βh ranging from $-0.5\beta h$ to $0.5\beta h$ and subsequently reaches full metal on both sides as shown in Fig. 2. The Young's modulus at any point across the thickness is calculated using the Young's modulus of ceramic E_c or metal E_m as follows:

$$E(n) = (E_c - E_m)V_c + E_m \tag{6}$$

where the ceramic volume fraction is written as follows:

$$\begin{cases} V_\mathrm{c} = \left[\dfrac{-|n| + 0.5h}{0.5(1-\beta)h}\right]^k, & -0.5h \le n \le -0.5\beta h \text{ or } 0.5\beta h \le n \le 0.5h \\ V_\mathrm{c} = 1, & -0.5\beta h \le n \le 0.5\beta h \end{cases} \tag{7}$$

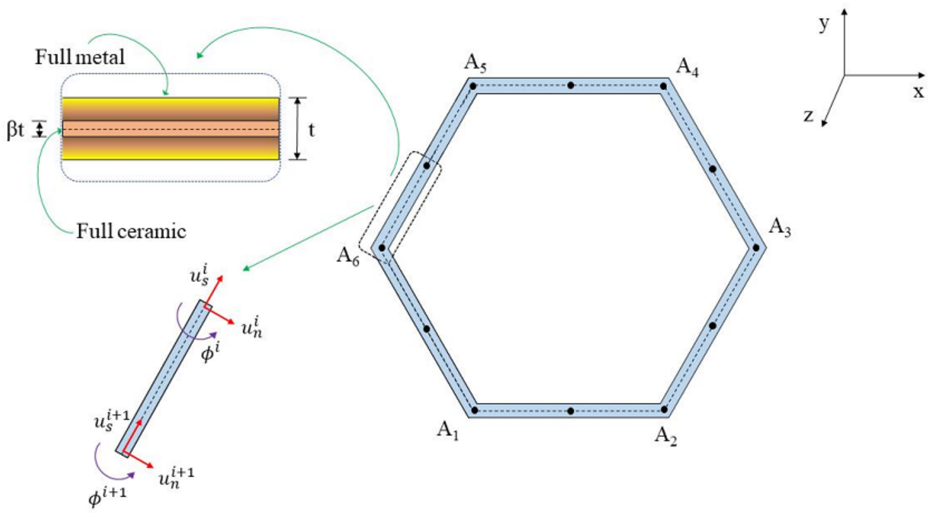

Figure 2. A hexagonal cross-section with DOFs on each edge and material distribution through the thickness direction

It is worth noting that the gradation index k can take on any value between 0 and infinity. When k reaches infinity, entire metal will cover the outside, while core ceramic βh will be positioned in the middle. If k is 0 , the material is now purely ceramic in all cross-section areas.

The internal strain energy within the whole domain V can be written as follows in terms of strains and stresses:

$$\mathbf{U} = \frac{1}{2}\int_V \boldsymbol{\sigma}^\mathrm{T}\epsilon \mathrm{d}V = \frac{1}{2}\int_V \epsilon^\mathrm{T}\mathbf{C}(n)\epsilon \mathrm{d}V \tag{8}$$

where $\mathbf{C}(n)$ is the material matrix for stress-strain.

2.2. *Beam frame modal*

Because the lowest eigenmodes frequently occur in thin-walled profiles, it has been discovered that the beam frame model can be used to obtain more accurate behaviors in practice. A multi-beam Euler element with a 3-degree-of-freedom node is considered on each edge of a given cross-section, as shown in Fig. 2.

The displacements are determined using the following formula:

$$\mathbf{U} = \mathbf{H}\mathbf{u} \tag{9}$$

where $\mathbf{u}$ denotes nodal displacement and $\mathbf{H}$ is the displacement interpolation matrix, which includes linear Lagrange and Hermite cubic interpolation functions.

As shown in Fig. 2, the nodal displacement vector for an element with nodes i^{th} and $(i+1)^{th}$ is defined as:

$$\mathbf{u} = \left\{ \begin{array}{cccccc} u_s^i & u_n^i & \phi^i & u_s^{i+1} & u_n^{i+1} & \phi^{i+1} \end{array} \right\}^{\mathrm{T}} \tag{10}$$

For the beam frame modal, the stiffness of an element can be calculated as:

$$\mathbf{K}_e^{\mathrm{BF}} = \int_V \mathbf{B}^{\mathrm{T}}\mathbf{C}\mathbf{B}\mathrm{d}V = \int_0^{l_e}\int_0^{b_{BF}}\int_{-h/2}^{h/2} \mathbf{B}^{\mathrm{T}}\mathbf{C}\mathbf{B}\mathrm{d}n\mathrm{d}z\mathrm{d}s \tag{11}$$

The explicit form of the stiffness matrix at the element level is:

$$\mathbf{K}_e^{\mathrm{BF}} = \begin{bmatrix} K_{11}^{\mathrm{BF}} & K_{12}^{\mathrm{BF}} & K_{13}^{\mathrm{BF}} & K_{14}^{\mathrm{BF}} & K_{15}^{\mathrm{BF}} & K_{16}^{\mathrm{BF}} \\ \vdots & K_{22}^{\mathrm{BF}} & K_{23}^{\mathrm{BF}} & K_{24}^{\mathrm{BF}} & K_{25}^{\mathrm{BF}} & K_{26}^{\mathrm{BF}} \\ \vdots & & K_{33}^{\mathrm{BF}} & K_{34}^{\mathrm{BF}} & K_{35}^{\mathrm{BF}} & K_{36}^{\mathrm{BF}} \\ \vdots & & & K_{44}^{\mathrm{BF}} & K_{45}^{\mathrm{BF}} & K_{46}^{\mathrm{BF}} \\ \vdots & & & & K_{55}^{\mathrm{BF}} & K_{56}^{\mathrm{BF}} \\ \text{sym.} & \dots & \dots & \dots & \dots & K_{66}^{\mathrm{BF}} \end{bmatrix} \tag{12}$$

Then the global stiffness matrix $\mathbf{K}^{\mathrm{BF}}$ is created by assembling element stiffness matrices $\mathbf{K}_e^{\mathrm{BF}}$ as follows:

$$\mathbf{K}^{\mathrm{BF}} = \sum_{e=1}^{N} \mathbf{T}_e^{\mathrm{T}}\mathbf{K}_e^{\mathrm{BF}}\mathbf{T}_e \tag{13}$$

After that, the equations are collected in a systematic manner to solve the standard eigenvalue problem:

$$\begin{bmatrix} \mathbf{K}^{\mathrm{BF}} & \mathbf{K}^{\mathrm{L}} \\ \text{sym.} & \mathbf{0} \end{bmatrix} \begin{Bmatrix} \mathbf{\Psi}^{\chi} \\ \boldsymbol{\varphi} \end{Bmatrix} = \lambda \begin{Bmatrix} \mathbf{\Psi}^{\chi} \\ \mathbf{0} \end{Bmatrix} \tag{14}$$

where $\mathbf{K}^{\mathrm{L}}, \mathbf{\Psi}^{\chi}, \boldsymbol{\varphi}$ and λ are represented as constraint matrix, nodal displacement vector, Lagrange multiplier and eigenvalue, respectively. The orthogonality of distortions is then handled over cross area A in terms of translational displacements and rotational angle as follows:

$$\begin{aligned}
&\iint_A \psi_s^{\chi}\psi_s^{x}\mathrm{d}n\mathrm{d}s = 0\\
&\iint_A \psi_s^{\chi}\psi_s^{y}\mathrm{d}n\mathrm{d}s = 0\\
&\iint_A \psi_s^{\chi}\psi_s^{\theta}\mathrm{d}n\mathrm{d}s = 0
\end{aligned} \tag{15}$$

where ψ_s^{χ} symbolizes distortion shape function for s-direction; $\psi_s^{x}, \psi_s^{y}, \psi_s^{\theta}$ represent in-plane rigid body translations for the x- and y-axis and torsional rotation about the z-axis, respectively.

Warping is then calculated based on constant shear flow conditions

$$\psi_z^{W}(s) = \int_s \left(\frac{\mathrm{d}\psi_s^{\chi}}{\mathrm{d}s}\mathrm{d}s \right) \mathrm{d}s \tag{16}$$

For out-of-plane rigid body modes, orthogonality is applied completely to the warping.

2.3. *Finite element formulations*

An element with two nodes i and j that correspond to two hexagonal cross-sections i and j is considered throughout the length of the beam. It should be noted that the planes comprising these sections are always defined to be normal to the beam center line, which leads to the center of each cross-section tracing from one end to the other end for all cross-sections. As a result, by using a sufficient number of straight elements, the technique allows the beam to vary in curvature.

Two sets of local coordinates are used to model thin-walled beam elements: (n_i, s_i, m_i) coordinate is defined as m_i is normal to cross-section plane, s_i is associated with contour direction, and n_i is orthogonal to s_i and m_i; $\left(n_i', s_i, m_i'\right)$ coordinate is defined as n_i' is normal to mid-surface of face i^{th}, and m_i' is orthogonal to $\left(n_i', s_i\right)$

The strain can now be rewritten using Eqs. (5) and (9) as follows:

$$\epsilon = \left\{ \begin{array}{c}
\left(\dfrac{\partial \mathbf{\Psi}_s(s)}{\partial s} - n\dfrac{\partial^2 \mathbf{\Psi}_n(s)}{\partial s^2} \right) \cdot \mathbf{H} \\
\mathbf{\Psi}_z(s)\dfrac{\partial \mathbf{H}}{\partial z} - n\mathbf{\Psi}_n(s)\dfrac{\partial^2 \mathbf{H}}{\partial z^2} \\
\mathbf{\Psi}_s(s)\dfrac{\partial \mathbf{H}}{\partial z} + \dfrac{\partial \mathbf{\Psi}_z(s)}{\partial s} \cdot \mathbf{H} - 2n\dfrac{\partial \mathbf{\Psi}_n(s)}{\partial s}\dfrac{\partial \mathbf{H}}{\partial z}
\end{array} \right\} \cdot \mathbf{u} = \mathbf{B}\mathbf{u} \tag{17}$$

in which $\mathbf{B}$ symbolizes the strain-displacement matrix.

The variation of total potential energy can be calculated in general form using Eq. (8) as:

$$\begin{aligned}
\delta\Pi &= \int_V \delta\mathbf{u}^{\mathrm{T}}\mathbf{B}^{\mathrm{T}}\mathbf{C}\mathbf{B}\mathbf{u}\mathrm{d}V - \int_V \mathbf{f}\delta\mathbf{u}\mathrm{d}V - \int_S \hat{\mathbf{t}}\delta\mathbf{u}\mathrm{d}S \\
&= \delta\mathbf{u}^{\mathrm{T}}\left(\int_V \mathbf{B}^{\mathrm{T}}\mathbf{C}\mathbf{B}\mathrm{d}V \right)\mathbf{u} - \mathbf{F}\delta\mathbf{u}
\end{aligned} \tag{18}$$

where $\mathbf{f}$ and $\hat{\mathbf{t}}$ denote the body force vector and surface traction on an area S, respectively.

The principle of minimum total potential energy is then applied, as follows:

$$\delta\Pi = 0 \tag{19}$$

All components must be performed in local coordinates to accurately describe stresses and strains. Natural coordinates (ξ, η, ζ) and direction cosine vectors $\hat{\mathbf{n}}'_{ij}$ of $\left(n'_i, s_i, m'_i\right)$ can be used to carry out this transformation as follows:

$$\nabla\mathbf{u}' = \left(\hat{\mathbf{n}}'_{ij}\right)^{\mathrm{T}} \cdot \nabla\mathbf{u} \cdot \hat{\mathbf{n}}'_{ij} \tag{20}$$

in which

$$\nabla\mathbf{u} = \mathbf{J}^{-1} \cdot \nabla\mathbf{u}_{\xi\eta\zeta} \tag{21}$$

with $\mathbf{J}$ denoting the Jacobian matrix.

3. Artificial neural network

Fig. 3 depicts a feed-forward neural network as an artificial neural network (ANN) with connections that do not form a cycle. This network is made up of N layers, with information flowing in only one direction from the input layer to the $(N-1)$ hidden layers and finally to the N^{th} output layer. Every two-unit has a connection in the neighboring layers, to which a connection weight is added. Each unit in the current layer receives a sum of the output values of the units in the previous layer multiplied by the corresponding connection weights and provides the activation function's output value for the sum as shown below.

$$O_j^p = f\left(U_j^p\right) = f\left(\sum_{i=1}^{n_p-1} w_{ji}^{p-1} \times O_j^{p-1} + \theta_j^p\right) \tag{22}$$

in which U_j^p and O_j^p represent the input and output values of the activation function of the j^{th} unit in the p^{th} layer, respectively; and w_{ji}^{p-1} denotes the connection weight between the i^{th} unit in the $(p-1)^{th}$ layer and the j^{th} unit in the p^{th} layer; θ_j^p denotes the bias of the j^{th} unit in the p^{th} layer; and f denotes the activation function.

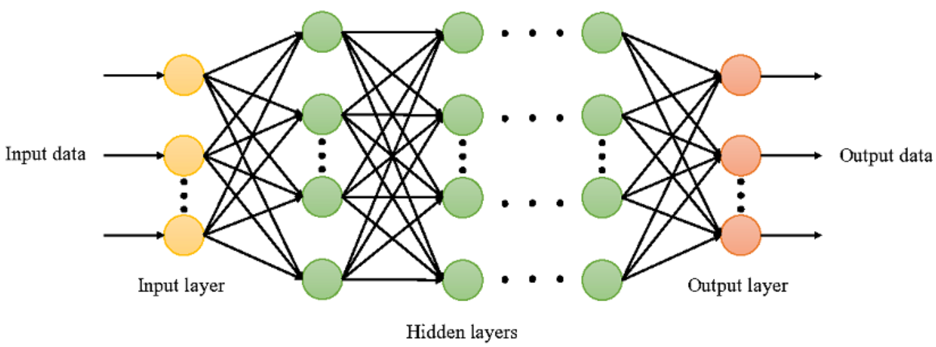

Figure 3. A feed-forward neural network structure

An identity mapping is used in this study for the activation function in the regression problem. In which Softplus which is a nonlinear function and widely used in ANN is used in this study. This activation function is described as follows:

$$f(x) = \ln\left(1 + e^x\right) \tag{23}$$

A training pattern is a pair of input and output data. A corresponding target data will be predicted from input data in the training pattern. These target data are compared to the corresponding output data to calculate the value of some predefined error functions. The mean square error (MSE) is one of the most commonly used methods for evaluating regression problems, and it is described as follows:

$$E_{MSE} = \frac{1}{n}\sum_{j=1}^{n}\left(O_j - T_j\right)^2 \tag{24}$$

in which n is the result of the number of training elements multiplied by the number of output neurons; O_j is the training pattern's output data; and T_j is the target data predicted from the training pattern's input data.

During the training phase, an optimizer of the gradient descent method minimizes a loss function similar to Eq. (24) to find the optimal weight parameter. In this study, Adam optimizer [19], which is a method for powerful stochastic optimization, is utilized. This method only requires first-order gradients and requires very little memory. Furthermore, its benefits combine those of two currently well-known methods: AdaGrad and RMSProp.

Mini-batch gradient descent (mBGD) [20] computes error for each of examples in the training data set. This technique is used to divide the training data set into small batches in order to compute model error and then update model coefficients. mBGD is the result of a trade-off between the efficiency of BGD and the robustness of stochastic gradient descent. Some benefits of mBGD have been discovered. The effectiveness of this approach is particularly evident in the memory without all training data because the frequency updated by this model is higher than BGD. mBGD could converge faster and avoid local solutions. Therefore, mBGD is used in this study.

4. Numerical example

In this study, a cantilever beam with a hexagonal cross-section shown in Fig. 1 as in study [10] in which cross-section axially varies from one end ($z = 0$) to the other end ($z = L$) is considered. The lengths of each edge of the two cross-sections at the ends are 30 mm and 10 mm, respectively. The length and thickness of the beam are 1.5 m and 2 mm, respectively. The skin-core-skin thickness β is 0.2. Al_2O_3-Al material is considered in which the properties of this material are given as: ceramic Al_2O_3: $E_c = 380$ GPa, $\nu_c = 0.3, \rho_c = 3960$ kg/m^3; metal Al: $E_m = 70$ GPa, $\nu_m = 0.3, \rho_m = 2702$ kg/m^3. A concentrated moment $M_z = 100$ Nm acting at the tip of the beam is considered. During the analysis performed by ANN, data sets are randomly created by the finite element analysis which is presented in study [10]. In which, the number of elements along the length of the beam is 50 and each edge of the cross-section consists of two elements. In the ANN, material distribution through thickness which is represented by k (gradation index in Eq. (7)) and thickness t are considered as inputs. In which the values of k are generated randomly by the uniform distribution (rand function) in the range $[0, 20]$ and t in the range $[1, 10]$ (mm) with a 0.1 mm jump. While the compliance $\left(C = \mathbf{u}^T\mathbf{Ku}\right)$ and twist angle along axial direction are considered as outputs. 1000 created data sets are used for training process to find optimal weights by using ANN. Based on these optimal weights, output data is predicted from an arbitrary input data. The dataset is divided into two groups: training and test sets, which correspond to 800 and 200 data pairs, respectively. In which the training dataset is used for learning and the test dataset is only used to assess performance, i.e. generalization of a process. Mini-batch size used in this study is ten. In the training phase, the influence of the number of hidden layers and epochs on the loss value is evaluated. In which, the number of nodes or units in each hidden layer is 100.

Three cases of a number of hidden layers (one, two, and three hidden layers) and six cases of epochs (500, 1000, 2000, 3000, 4000, and 5000 epochs) are considered for this investigation. Table 1 displays the obtained mean square error (MSE), mean absolute percentage error (MAPE) for training and test sets and training time.

Table 1. MSE and MAPE for training and test sets, as well as training time with a variety of hidden layers and epochs

Hidden layer structure		100					
Epochs		500	1000	2000	3000	4000	5000
MSE	Training	9.11E-04	2.06E-04	1.60E-04	1.12E-04	8.52E-05	6.30E-05
	Test	9.98E-04	2.36E-04	1.74E-04	1.27E-04	9.65E-05	6.91E-05
MAPE	Training	5.84E+00	2.40E+00	2.16E+00	1.83E+00	1.64E+00	1.29E+00
	Test	6.02E+00	2.55E+00	2.23E+00	1.98E+00	1.79E+00	1.39E+00
Time (second)		25	52	98	154	215	264
Hidden layer structure		100-100					
Epochs		500	1000	2000	3000	4000	5000
MSE	Training	5.89E-05	3.50E-05	1.67E-05	1.39E-05	3.27E-06	1.67E-06
	Test	5.69E-05	3.13E-05	1.27E-05	1.02E-05	3.38E-06	1.91E-06
MAPE	Training	1.09E+00	8.16E-01	6.34E-01	5.38E-01	3.87E-01	2.37E-01
	Test	1.16E+00	8.65E-01	6.29E-01	5.43E-01	3.84E-01	2.38E-01
Time (second)		45	98	196	286	378	539
Hidden layer structure		100-100-100					
Epochs		500	1000	2000	3000	4000	5000
MSE	Training	4.58E-05	2.65E-05	5.49E-06	3.43E-06	9.44E-07	1.65E-07
	Test	3.96E-05	2.38E-05	5.06E-06	3.67E-06	8.38E-07	1.85E-07
MAPE	Training	8.54E-01	7.34E-01	4.56E-01	4.56E-01	1.22E-01	6.08E-02
	Test	9.79E-01	7.40E-01	4.60E-01	4.66E-01	1.19E-01	6.83E-02
Time (second)		72	119	237	378	456	579

From the table, it can be seen that as the number of hidden layers or epochs increases, the MSE and MAPE gradually decrease, implying that the accuracy increases. The best results are obtained by three hidden layers and 5000 epochs with MSE 1.6527E-07 for training and 1.8521E-07 for testing. Besides, the accuracy reaches 99.94% for training and 99.93% for testing. Fig. 4 depicts the obtained convergence history of the loss function of the training and test sets in the best case with three hidden layers and 5000 epochs. From the figure, it can be seen that training and test loss converge to zero and they remain stable at the last stage of the process. Therefore, optimum weights can be found.

To verify the accuracy of the proposed method, the configuration of the final ANN with three hidden layers and 5000 epochs is used to predict beam behavior. Results obtained by this model are compared to those of finite element method (FEM) [10]. Inputs are gradation indices with $k = 0, 1, 5$ and 10; and thickness t is chosen to be 0.2. These input data sets are unseen data and not included in the train and test data sets. In terms of outputs, Fig. 5 shows a comparison of the twist angle along

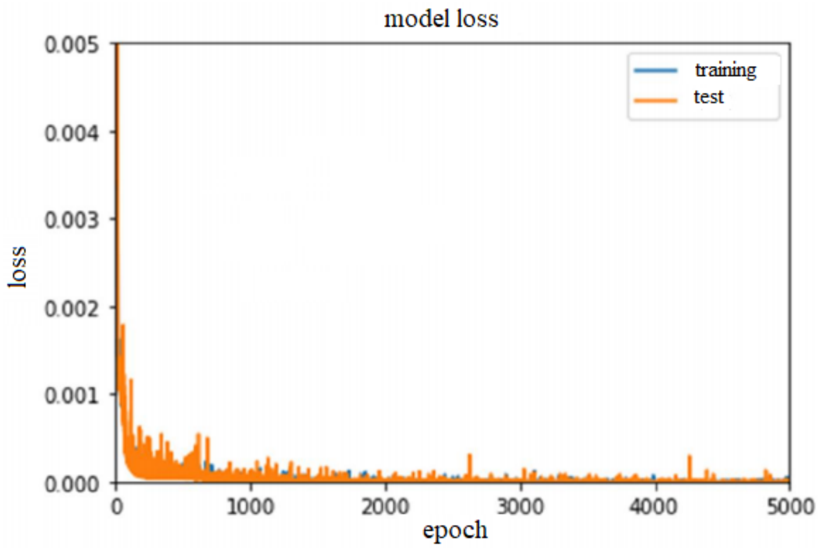

Figure 4. The convergence history of loss function of the beam under concentrated moment obtained by ANN with three hidden layers and 5000 epochs

the axial direction with various gradation indices obtained by the proposed method and FEM. From the table, it can be seen that the results obtained by the proposed method agree well with the results obtained by the FEM. Fig. 6 also shows the compliance values obtained by both methods in those cases. As shown in the figure, the values obtained by the two methods are almost identical. Therefore, the accuracy of the present method has been demonstrated through numerical examples.

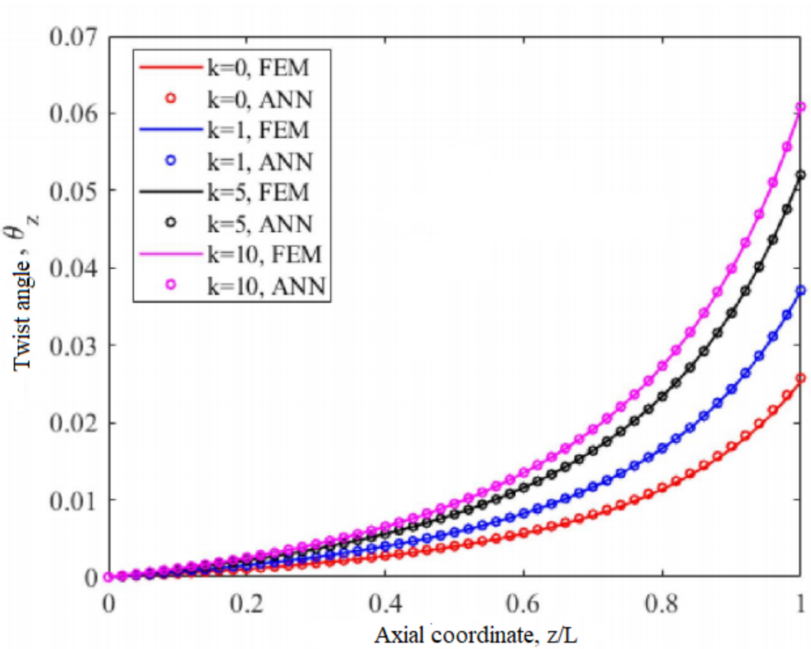

Figure 5. Twist angle variation with respect to axial coordinate of the beam obtained by FEM and ANN

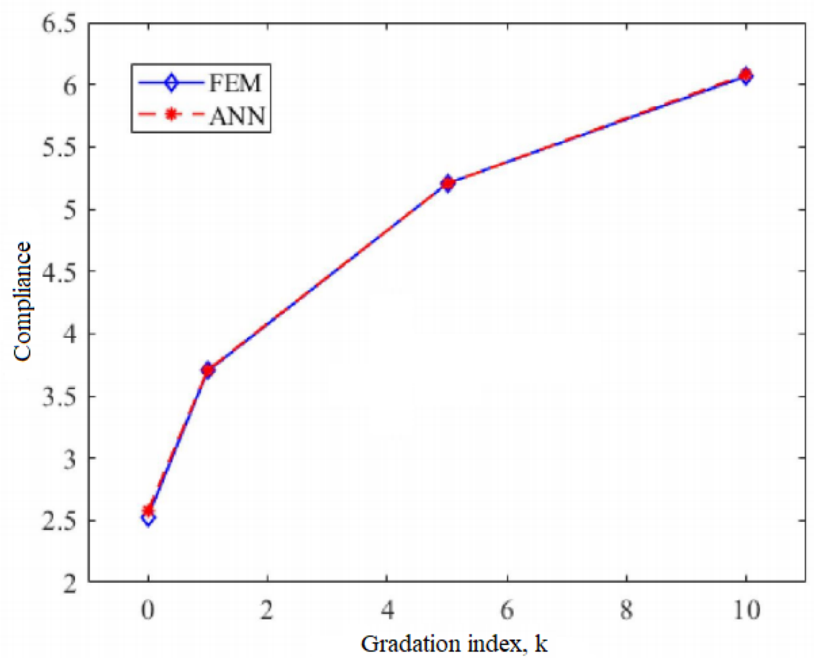

Figure 6. Compliance of the beam obtained by FEM and ANN

5. Conclusions

In this paper, we have presented a non-traditional computational approach based on ANN for analyzing the mechanical behavior of non-uniform hexagonal cross-sections for thin-walled functionally graded beams under static loading. The ANN is used as an alternative to the FEM to reduce the computational cost in the optimization problems. Gradation index and thickness are considered inputs while the compliance and displacement are considered as outputs of the ANN setting. To obtain optimal weights, the training process is not computationally expensive. Based on these obtained optimal weights, the compliance and twist angle along the axial direction are correctly predicted by the ANN, reflecting the accuracy and efficiency of the present formulation.

This study can be extended to find material distribution or the size and shape of non-uniform cross-sections for thin-walled functionally graded beams through optimization. Furthermore, the use of ANN for more complex structures is expected.

Acknowledgements

This research is funded by Vietnam Ministry of Education and Training (MOET) under grant number B2021-VGU-04.

References

[1] Bai, Y., Wang, J., Liu, Y., Lin, X. (2017). Thin-Walled CFST Columns for Enhancing Seismic Collapse Performance of High-Rise Steel Frames. *Applied Sciences*, 7(1):53.

[2] Yang, N., Bai, F. (2017). Damage Analysis and Evaluation of Light Steel Structures Exposed to Wind Hazards. *Applied Sciences*, 7(3):239.

[3] Lanc, D., Vo, T. P., Turkalj, G., Lee, J. (2015). Buckling analysis of thin-walled functionally graded sandwich box beams. *Thin-Walled Structures*, 86:148–156.

[4] Nguyen, T.-T., Thang, P. T., Lee, J. (2017). Lateral buckling analysis of thin-walled functionally graded open-section beams. *Composite Structures*, 160:952–963.

[5] Nguyen, T.-T., Lee, J. (2017). Optimal design of thin-walled functionally graded beams for buckling problems. *Composite Structures*, 179:459–467.

[6] Librescu, L., Oh, S.-Y., Song, O. (2005). Thin-Walled Beams Made of Functionally Graded Materials and Operating in a High Temperature Environment: Vibration and Stability. *Journal of Thermal Stresses*, 28 (6-7):649–712.

[7] Vlasov, V. Z. (1961). *Thin-walled elastic beams*. 2nd Revised Edition. Israel Program for Scientific Translations.

[8] Tews, R., Rachowicz, W. (2009). Application of an automatic hp adaptive Finite Element Method for thin-walled structures. *Computer Methods in Applied Mechanics and Engineering*, 198(21-26):1967–1984.

[9] Rank, E., Kollmannsberger, S., Sorger, C., Düster, A. (2011). Shell Finite Cell Method: A high order fictitious domain approach for thin-walled structures. *Computer Methods in Applied Mechanics and Engineering*, 200(45-46):3200–3209.

[10] Nguyen, T.-T., Nguyen, N.-L., Lee, J., Nguyen, Q.-H. (2021). Analysis of non-uniform polygonal cross-sections for thin-walled functionally graded straight and curved beams. *Engineering Structures*, 226: 111366.

[11] Nguyen, T.-T., Nguyen, Q.-H., Le, T. D., Le, H. D. (2021). General non-uniform quadrilateral cross-sections for thin-walled FG sandwich beams. *Journal of Science and Technology in Civil Engineering (STCE) - NUCE*, 15(2):90–100.

[12] Vesperini, F., Vecchiotti, P., Principi, E., Squartini, S., Piazza, F. (2018). Localizing speakers in multiple rooms by using Deep Neural Networks. *Computer Speech & Language*, 49:83–106.

[13] Do, D., Lee, D., Lee, J. (2019). Material optimization of functionally graded plates using deep neural network and modified symbiotic organisms search for eigenvalue problems. *Composites Part B: Engineering*, 159:300–326.

[14] Ha, L. H., Hung, L., Trung, L. Q. (2018). A risk assessment framework for construction project using artificial neural network. *Journal of Science and Technology in Civil Engineering (STCE) - NUCE*, 12 (5):51–62.

[15] Hung, D. V., Hung, H. M., Anh, P. H., Thang, N. T. (2020). Structural damage detection using hybrid deep learning algorithm. *Journal of Science and Technology in Civil Engineering (STCE) - NUCE*, 14 (2):53–64.

[16] Hung, T. V., Viet, V. Q., Thuat, D. V. (2019). A deep learning-based procedure for estimation of ultimate load carrying of steel trusses using advanced analysis. *Journal of Science and Technology in Civil Engineering (STCE) - NUCE*, 13(3):113–123.

[17] Hung, D. V., Thang, N. T., Dat, P. X. (2021). Probabilistic pushover analysis of reinforced concrete frame structures using dropout neural network. *Journal of Science and Technology in Civil Engineering (STCE) - NUCE*, 15(1):30–40.

[18] Nhu, N. T. H., Binh, T. A., Hung, H. M. (2020). A three-dimensional model for rain-wind induced vibration of stay cables in cable-stayed bridges. *Journal of Science and Technology in Civil Engineering (STCE) - NUCE*, 14(1):15–27.

[19] Kingma, D. P., Ba, J. (2017). *Adam: A Method for Stochastic Optimization*. arXiv:14126980.

[20] Hinton, G. E. (2012). A Practical Guide to Training Restricted Boltzmann Machines. In *Lecture Notes in Computer Science*, Springer Berlin Heidelberg, 599–619.